ANNUAL REVIEWS

Annual Review of Earth and Planetary Sciences

Hydration and Dehydration in Earth's Interior

Eiji Ohtani

Department of Earth Science, Graduate School of Science, Tohoku University, Sendai 980-8578, Japan; email: eohtani@tohoku.ac.jp

ANNUAL REVIEWS CONNECT

www.annualreviews.org

- Download figures
- Navigate cited references
- Keyword search
- Explore related articles
- Share via email or social media

Keywords

hydration, dehydration, water budget, water circulation, high pressure, high temperature

Abstract

Hydrogen and deuterium isotopic evidence indicates that the source of terrestrial water was mostly meteorites, with additional influx from nebula gas during accretion. There are two Earth models, with large (7–12 ocean masses) and small (1–4 ocean masses) water budgets that can explain the geochemical, cosmochemical, and geological observations. Geophysical and mineral physics data indicate that the upper and lower mantles are generally dry, whereas the mantle transition zone is wetter, with heterogeneous water distribution. Subducting slabs are a source of water influx, and there are three major sites of deep dehydration: the base of the upper mantle, and the top and bottom of the lower mantle in addition to slabs in the shallow upper mantle. Hydrated regions surround these dehydration sites. The core may be a hidden reservoir of hydrogen under the large water budget model.

- Earth is a water planet. Where and when was water delivered, and how much? How does water circulate in Earth? This review looks at the current answers to these fundamental questions.

1. INTRODUCTION

Earth is a water planet. Water controls the evolution and dynamics of Earth because very small amounts of water can modify the physical properties of Earth materials. Water reduces melting temperatures to generate magmatism/volcanism; enhances diffusion; weakens Earth's materials, which is called hydrolytic weakening; and promotes recrystallization.

The minerals in the mantle transition zone (MTZ), wadsleyite and ringwoodite, can contain relatively large amounts of water: up to 1–2 wt%. However, whether these water reservoirs in the MTZ are filled is debated, making it important to estimate the water content of Earth's interior. Estimates can be based on geophysical observations, such as seismic velocity, electrical conductivity, and geodetic data in combination with mineral physics and geochemical data.

The timing and magnitude of water delivery to Earth are unresolved issues. Geochemical evidence and numerical simulation of Earth's accretion processes constrain the total water budget of the interior. This review focuses on the current understanding of the total water budget, water circulation and storage, and hydration and dehydration sites in Earth.

2. ORIGIN OF WATER IN EARTH AND PLANETS

2.1. Origin of Earth's Water

The origin and timing of water delivery to Earth are unresolved. Several sources have been suggested for the origin of Earth's water, including primitive planetesimals formed from nebula gas, meteorites, and comets. The isotopic ratio of hydrogen and deuterium—i.e., the D/H ratio—provides a diagnostic tool that helps distinguish the origin of water in Earth. The D/H ratio is represented by the δ notation, which describes variation of the measured ratio relative to a standard; the D/H ratio of terrestrial oceanic water [standard mean ocean water (SMOW)] is expressed as permil (‰) and is defined as $\delta D = [(R_x - R_{STD})/R_{STD}] \times 10^3$, where $R_x = (D/H)_x$ (the D/H ratio of the sample x) and R_{STD} is the D/H ratio in SMOW. Water in the ocean has $\delta D = 0$ by definition.

Bulk Earth has a D/H ratio, δD, of about -37‰ (e.g., Hallis 2017). Depending on the source of water, δD in the oceanic and continental mantle lithospheres varies from -60‰ to -130‰ (e.g., Bell & Ihinger 2000). In certain igneous rocks whose sources originate from deep regions of the mantle, the ratio is significantly lower than in igneous rocks from other sources. For example, Baffin Island lavas, which also have high $^3He/^4He$, have $\delta D \leq -217$‰ (Hallis et al. 2015), suggesting the existence of a primitive water source in Earth's interior. Structurally bound water in carbonaceous chondrites has $\delta D \sim -101 \pm 60$‰, close to the terrestrial value (Robert 2006). Solar nebula gas has $\delta D = -872 \pm 22$‰ (Geiss & Gloeckler 2003), which is close to that of Jupiter and Saturn. Water from comets generally has very high D/H ratios [$\delta D = +926$‰ (e.g., Bockelée-Morvan et al. 2015)], although some comets possess ratios close to terrestrial values [$\delta D \sim 34 \pm 154$‰ for comet Hartley 2 (Hartogh et al. 2011)].

Based on comparison of the D/H ratios of terrestrial and extraterrestrial water, water in Earth is widely considered to have been delivered by accretion of carbonaceous chondritic materials (e.g., Alexander et al. 2012). Small amounts of nebula components may exist in terrestrial water, as observed in the low D/H values of some rocks from Earth's deep interior (e.g., Hallis et al. 2015). The contribution from comets is considered limited because their collision probability with Earth is very small (Morbidelli et al. 2012).

The amount of water accreted early in Earth history has been estimated by numerical simulation. Abe & Matsui (1986) simulated the accretion process after blow off of nebula gas and found that the primitive atmosphere contained water vapor equivalent to the present ocean mass.

A simulation by Rubie et al. (2015) suggested that 1,000 ppm (about 4 ocean masses) of water were delivered during the accretion of Earth.

An accretion model of Earth, within nebula gas, has been suggested by Hayashi et al. (1979). Some noble gases, particularly ^{3}He and ^{22}Ne in terrestrial rocks, are considered to have been derived from the solar nebula. These noble gases are believed to have dissolved from the primordial atmosphere into the magma ocean during accretion, a process called nebular ingassing (Sharp 2017). Olsen & Sharp (2019) modeled the ingassing process during Earth's accretion and suggested that the magma ocean ingassed about 7 ocean masses of water and hydrogen, along with ^{3}He and other light noble gases. Wu et al. (2018) presented a model of nebular ingassing of hydrogen and suggested that Earth possesses water equivalent to roughly 2 oceans in the mantle and 5 oceans in the core. Marty & Yokouchi (2006) estimated the water content of Earth as 350–1,000 ppm (1–4 ocean masses), whereas Marty (2012) re-estimated it as 1,000–3,000 ppm (4–12 ocean masses) based on abundances of noble gases and volatiles. McDonough (2014) estimated that bulk Earth contains hydrogen at about 2,600 ppm (10 ocean masses) with 0.06 wt% (about 7 ocean masses) in the core. Different models for the water budget of Earth are shown in **Table 1**.

2.2. Origin and History of the Oceans

The timing of water delivery is one of the most important issues related to the origin of terrestrial water. Several possibilities include water being delivered as nebula and C1 chondritic components during accretion and giant impact, as the late veneers from meteoritic bombardments, and throughout geological history by comets. Changes of ocean mass over time have been estimated based on geological constraints on the early ocean. Recent estimations of the influx of ocean water are equal to or greater than the outgassing flux, resulting in constant or secular reductions of the ocean mass (e.g., Peacock 1990, Wallace 2005, van Keken et al. 2011), although an early model of ocean formation indicated gradual degassing and an increase in ocean water with time (Rubey 1951). There is no consensus on the secular change of the ocean mass due to the lack of robust evidence. The following geodynamic studies favor reduction of ocean water over time: Korenaga (2011) modeled water circulation due to plate tectonics and estimated the magnitude of net influx of water into the mantle assuming constant continental freeboard. This net influx is equivalent to 1 ocean mass over 4.5 billion years. This positive influx model by Korenaga (2011) implies a dry mantle and a voluminous ocean, at least twice the present ocean mass, at the beginning of Earth's history. Nakagawa et al. (2018), however, calculated the total mass of the early ocean and constrained the total amount of water in Earth's system using numerical calculation of thermochemical convection and water migration from the early to present Earth. They concluded that a bulk Earth water equivalent of 9 to 12 ocean masses is required to maintain the ocean throughout Earth's history.

3. STABILITY OF HYDROUS MINERALS IN THE MANTLE

3.1. High-Pressure Hydrous Minerals in the Mantle

There are various hydrous minerals in the mantle that have very important roles for water transport and cycling in Earth. Here we summarize the mineralogical and physical properties of these hydrous minerals and their stability conditions in the upper mantle, MTZ, and lower mantle.

3.1.1. Upper mantle and mantle transition zone. Many hydrous minerals such as chlorite, amphibole, and serpentine are known to exist in the crust and slabs descending into the upper

Table 1 Water budget in Earth

Region	Water budget (1 ocean mass ~1.4 x 10^{24} g)	Water contents (ppm)	Method(s)	Reference(s)
Bulk Earth				
Bulk Earth	1~1.5	250–400	Numerical calculation of accretion	Abe & Matsui 1986
	4	1,000	Numerical calculation of accretion	Rubie et al. 2015
	7 (in the mantle)	1,750	Numerical calculation of accretion	Olsen & Sharp 2019
	7.8 (surface ~1, mantle 2, core 4.8)	2,000	Numerical calculation of accretion	Wu et al. 2018
	9~12	2,120~2,830	Numerical calculation of convection	Nakagawa et al. 2018
	1~4	300~1,000	Geochemistry	Marty & Yokouchi 2006
	4~12	1,000~3,000	Geochemistry	Marty 2012
	10	2,500	Geochemistry/cosmochemistry	McDonough 2014
	2.6~100	640~36,600	Geochemistry/cosmochemistry/ geophysical observations/mineral physics	Peslier et al. 2017
	2.7~16	680~3,800	Numerical calculation of accretion/ geochemistry/cosmochemistry/ geophysical observations/mineral physics	Present estimation
Ocean/Crust				
Ocean	1	100% (1.4 × 10^{21} kg)	Hydrology/geodesy	Peslier et al. 2017
Crust	0.3~0.4	15,000–20,000	Geochemistry/petrology	Peslier et al. 2017
Mantle				
Mantle	7	2,500	Numerical calculation of accretion	Olsen & Sharp 2019
	2	700	Numerical calculation of accretion	Wu et al. 2018
	2	700	Numerical calculation of convection	Korenaga 2011
	1.1~7.4	382~2,564	Electrical conductivity/seismology/ mineral physics	Peslier et al. 2017
	1.3~6.9	490~2,400	Electrical conductivity/seismology/ geodesy/mineral physics	Present estimation
Upper mantle				
Upper mantle	0.04	100	Electrical conductivity sounding/mineral physics	Karato 2011
	<0.4	<1,000	Electrical conductivity sounding/ mineral physics	Yoshino & Katsura 2013
Cratonic mantle lithosphere	ND	20	Electrical conductivity sounding/mineral physics	Jones et al. 2013
Oceanic mantle lithosphere	ND	<50	Electrical conductivity sounding/mineral physics/geochemistry	Pommier 2014

(Continued)

Table 1 (*Continued*)

Region	Water budget (1 ocean mass ~1.4 x 10^{24} g)	Water contents (ppm)	Method(s)	Reference(s)
Asthenosphere (~300 km depth)	ND	400	Electrical conductivity sounding/ mineral physics/geochemistry	Pommier 2014
Slab in the upper mantle	ND	300–3,000	Seismology/mineral physics/ geochemistry	Peslier et al. 2017
	ND	300–3,000	Seismology/mineral physics/ geochemistry	Present estimation
Upper mantle	0.08	200	Electrical conductivity sounding/mineral physics/geochemistry	Peslier et al. 2017
	0.04~0.08	100~200	Electrical conductivity sounding/mineral physics/geochemistry	Present estimation
MTZ				
MTZ	<1	Dry (<3,450)	Seismology/mineral physics	Houser 2016
	2.9~5.8	10,000~20,000 (water saturated)	Geodetic and gravity/viscosity/mineral physics	Fei et al. 2017, Mitrovica & Forte 2004, Soldati et al. 2009
	0.29	1,000	Electrical conductivity sounding/ mineral physics	Karato 2011
	0.29~0.87	1,000~3,000	Electrical conductivity sounding/ mineral physics	Yoshino & Katsura 2013
Stagnant slab beneath the Philippine Sea in MTZ	ND	2,000	Seismology/mineral physics	Suetsugu et al. 2010
Stagnant slab beneath the Philippine Sea and western-most Japan	ND	10,000~40,000	Seismology/depth of 660 km discontinuity and V_P tomography/ mineral physics	Suetsugu et al. 2006
Stagnant slab beneath the Philippine Sea in MTZ	0.75	6,000	Seismology/mineral physics	Houser 2016
Upper part of MTZ	~0.73	~5,000	Seismology (impedance contrast)/ mineral physics	Chambers et al. 2005, Buchen et al. 2018
	0.145	1,000	Electrical conductivity sounding/mineral physics	Yoshino & Katsura 2013
	0.145	1,000	Electrical conductivity sounding/mineral physics	Karato 2011
Lower MTZ	0.145–0.73	1,000–5,000	Electrical conductivity sounding/mineral physics	Yoshino & Katsura 2013
	0.145	1,000	Electrical conductivity sounding/mineral physics	Karato 2011
MTZ beneath Northwest China and the Philippine Sea	ND	5,000~10,000	Electrical conductivity sounding/ mineral physics	Yoshino & Katsura 2013, Karato 2011

(*Continued*)

Table 1 (*Continued*)

Region	Water budget (1 ocean mass ~1.4 x 10²⁴ g)	Water contents (ppm)	Method(s)	Reference(s)
MTZ beneath Mariana	ND	3,000	Electrical conductivity sounding/ seismology/mineral physics	Koyama et al. 2006
MTZ beneath Europe	ND	Dry < 1,000	Electrical conductivity sounding/ seismology/mineral physics	Utada et al. 2009
MTZ beneath the Philippine Sea	ND	5,000~10,000	Electrical conductivity sounding/ seismology/mineral physics	Utada et al. 2009
MTZ	0.9~1.5	3,140~5,100	Electrical conductivity sounding/ seismology/mineral physics	Peslier et al. 2017
	0.29~5.8	1,000~20,000	Electrical conductivity sounding/ seismology/mineral physics	Present estimation
Lower mantle				
Eastern Asia	>2	>1,000 (over-saturated)	Seismology/attenuation	Lawrence & Wysession 2006
Normal lower mantle	Dry ≪ 2	Dry ≪ 1,000	Seismology/attenuation	Lawrence & Wysession 2006
LLSVP	1	19,000 (12 vol% δ-phase)	Seismology/mineral physics	Ohira 2018
	2.6	50,000 (35 vol% δ-phase)	Seismology/mineral physics	Mashino et al. 2016
Lower mantle	0.2~4.5?	100~2,000	Seismology/mineral physics	Peslier et al. 2017
	1	460	Seismology/mineral physics	Present estimation
Core				
Core	4.8[a]	340[b]	Numerical calculation of accretion	Wu et al. 2018
	7.5[a]	600[b]	Geochemistry	McDonough 2014
	124–248 (maximum)[a]	10,000~20,000[b]	Mineral physics/density deficit	Terasaki et al. 2012
	Not the major candidate	Minor H	NRIXS/⁵⁷Fe isotope/mineral physics	Shahar et al. 2016
	80 (±31) (maximum)[a]	6,450 (±25,000) (maximum)[b]	Mineral physics/neutron diffraction	Ikuta et al. 2019
	0.2~90 (maximum)[a]	16~7,200 (maximum)[b]	Geochemistry, seismology/mineral physics/density deficit	Peslier et al. 2017
	0~7.5[a]	0~600[b]	Numerical calculation of accretion, geochemistry, seismology/mineral physics/density deficit, NRIXS/⁵⁷Fe isotope/mineral physics	Present estimation

Mass of regions in Earth: ocean, 1.4×10^{21} kg; crust, 28.12×10^{21} kg; upper mantle, 584×10^{21} kg; MTZ, 400×10^{21} kg; lower mantle, $3,030 \times 10^{21}$ kg; core, $1,928.7 \times 10^{21}$ kg; LLSVP, 1.9% of mantle, i.e., 76.3×10^{21} kg (Burke et al. 2008). Abbreviations: LLSVP, large low-shear velocity province; MTZ, mantle transition zone; ND, not determined.

[a]The amount of hydrogen in the core that corresponds to a multiple of the ocean mass excluding oxygen.

[b]Hydrogen contents (ppm).

Table 2 Water contents and stable pressure and temperature conditions of hydrous minerals

Mineral name	Formula	H$_2$O wt%	Pressure and temperature (GPa/K)	Reference(s)
10 Å phase	Mg$_3$Si$_4$O$_{14}$H$_6$	13	6.7/923	Fumagalli et al. 2001
Phase A	Mg$_7$Si$_2$O$_8$(OH)$_6$	12	6$\sim$14/1,073	Ringwood & Major 1967
Phase B	Mg$_{12}$Si$_4$O$_{19}$(OH)$_2$	2.4	11$\sim$16/1,273	Ringwood & Major 1967
Superhydrous phase B = phase C	Mg$_{12}$Si$_3$O$_{12}$(OH)$_4$	5.8	20/1,273	Pacalo & Parise 1992
Phase D = phases F, G	Mg$_{1.14}$Si$_{1.73}$H$_{2.81}$O$_6$	14.5$\sim$18	15$\sim$40/1,273	Ohtani et al. 1997
Phase E	Mg$_{2.3}$Si$_{1.25}$H$_{2.4}$O$_6$	11.4	15/1,173	Kanzaki 1991
HAPY (hydrous Al-bearing pyroxene)	Mg$_{2.1}$Al$_{0.9}$(OH)$_2$Al$_{0.9}$Si$_{1.1}$O$_6$	7	5.4/720	Gemmi et al. 2011
23 Å phase	Mg$_{11}$Al$_2$Si$_4$O$_{16}$(OH)$_{12}$	12.1	10/1,000	Cai et al. 2015
11.5 Å phase	Mg$_6$Al(OH)$_7$(SiO$_4$)$_2$	13	6.5/700	Gemmi et al. 2016
Hyso phase (hydrous solosilicate)	Mg$_3$Al(OH)$_3$Si$_2$O$_7$	8.5	6.5/700	Gemmi et al. 2016
Phase egg	AlSiO$_3$OH	7.5	13$\sim$30/$\sim$1,873	Sano et al. 2004, Abe et al. 2018
Phase δ	AlOOH	15	$\sim$142/$\sim$2,500	Duan et al. 2018
Phase δ-H solid solution (aluminous phase H)	(Mg$_{0.07}$Si$_{0.07}$Al$_{0.86}$)OOH	12.8	$\sim$128/$\sim$2,190	Suzuki et al. 2000, Ohira et al. 2014
Phase H	MgSiO$_2$(OH)$_2$	15	40$\sim$60/1,600	Ohtani et al. 2014
Pyrite-type FeOOH	FeOOH$_x$	14	100/2,000	Nishi et al. 2017

mantle. Dehydration of these minerals as the slab descends produces fluids that transport volatile and large iron lithophile elements from the slab to the overlying mantle (e.g., Mysen 2018, 2019) and so create volcanism in island arcs and earthquakes in subduction zones (e.g., Hacker et al. 2003).

Several high-pressure hydrous phases have been reported in the upper mantle and MTZ. Typical hydrous phases stable at high pressures include dense hydrous magnesium silicates (DHMS), also known as the alphabet phases (Ringwood & Major 1967). Pioneering research by Ringwood & Major (1967) revealed the existence of high-pressure hydrous phases, which they referred to as phases A, B, and C. Phase D was later reported by Liu (1987). Pacalo & Parise (1992) reported a hydrous phase with the composition Mg$_{10}$Si$_3$O$_{14}$(OH)$_4$ and named it as superhydrous phase B, which proved to be identical to the previously identified phase C. Kanzaki (1991) reported that phase E and phase F are stable at 13–17 GPa, while Ohtani et al. (1997) reported a hydrous phase at even higher pressure and named it phase G. Later studies revealed that phase F and phase G are similar to phase D. Currently, the name of superhydrous phase B is used in place of phase C, and phase D commonly refers to phases F and G (see **Table 2**).

In subducting slabs, water is mainly stored in hydrous phases that change progressively with depth. It is stored in chlorite and serpentine and then in 10 Å phase (TAP) (Fumagalli et al. 2001). Water can be carried further by phase A and is trapped in phase E after dehydration of phase A, and then in superhydrous phase B along a low-temperature slab geotherm. The sequence of hydrous phases with depth is shown in **Figure 1**.

Recently, several new aluminum-bearing hydrous phases such as the HAPY (hydrous Al-bearing pyroxene) phase, Mg$_{2.1}$Al$_{0.9}$(OH)$_2$Al$_{0.9}$Si$_{1.1}$O$_6$ (Gemmi et al. 2011); the 11.5 Å phase,
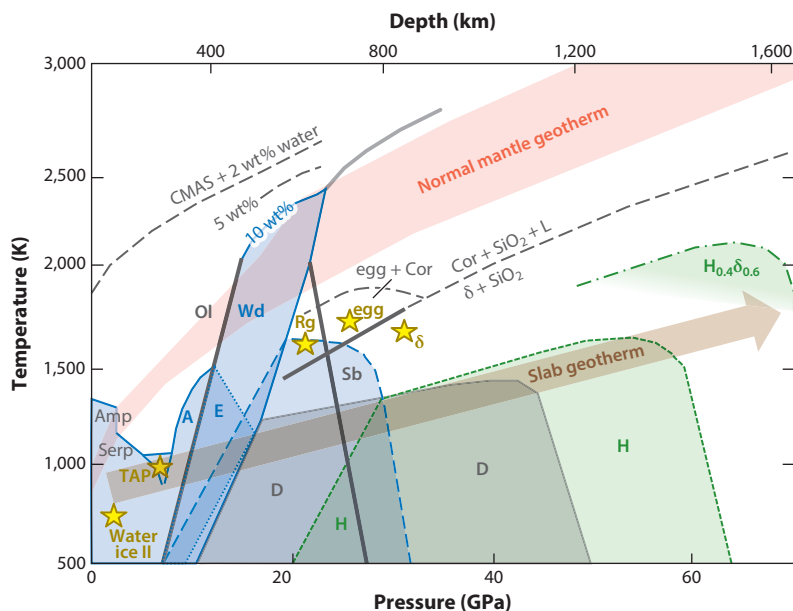
Figure 1

Hydrous minerals in Earth's mantle. Yellow stars are the stable conditions of inclusions in deep-seated diamonds, such as water ice II (Tschauner et al. 2018), TAP (Huang et al. 2020), Rg (Pearson et al. 2014), egg (Wirth et al. 2007), and δ (Wirth et al. 2007, Kaminsky 2017). The stability fields of hydrous phases are explained in Section 3. Abbreviations: δ, phase δ-AlOOH; A, phase A; Amp, amphibole; Cor, corundum; D, phase D; E, phase E; egg, phase egg; H, phase H; $H_{0.4}\delta_{0.6}$, phase H-δ solid solution; Ol, olivine; Rg, ringwoodite; Sb, superhydrous phase B; Serp, serpentine; TAP, 10 Å phase; Wd, wadsleyite.

$Mg_6Al(OH)_7(SiO_4)_2$; the Hyso (hydrous solosilicate) phase, $Mg_3Al(OH)_3Si_2O_7$ (Gemmi et al. 2016); and the 23 Å phase, $Mg_{11}Al_2Si_4O_{16}(OH)_{12}$ (Cai et al. 2015), have been discovered in the pressure range beyond the stability field of chlorite. These phases may exist in subducting slabs, although their stability fields within the slabs are not yet clear. The mineralogical properties of hydrous phases in the mantle are summarized in **Table 2**. Other hydrous phases in the upper mantle are summarized elsewhere (e.g., Ohtani et al. 2018).

3.1.2. Hydrous phases in the lower mantle. Superhydrous phase B is stable to the top of the lower mantle and then decomposes into ferropericlase, bridgmanite, and phase D (Ohtani et al. 2003). Dissolution of alumina in phase D expands its stability field (e.g., Xu & Inoue 2019). Phase egg ($AlSiO_3OH$) (Eggleton et al. 1978, Schmidt 1995), discovered as an inclusion in diamond (Wirth et al. 2007), is stable throughout the MTZ and decomposes to phase δ-AlOOH and stishovite at the top of the lower mantle (Sano et al. 2004, Abe et al. 2018). Suzuki et al. (2000) discovered phase δ-AlOOH as a reaction product of pyrope and water at around 20 GPa. This phase can dissolve Mg and Si in its structure to form a solid solution of $AlOOH-MgSiO_2(OH)_2$. Phase δ-AlOOH has a wide stability field to the base of the lower mantle and is considered to be a major carrier of water to the lower mantle (Duan et al. 2018).

Phase H, the end member of the solid solution $MgSiO_2(OH)_2$, is stable to 60 GPa and 1,600 K (Nishi et al. 2014, Ohtani et al. 2014). Ohira et al. (2014) reported a reaction between alumina-bearing bridgmanite/postperovskite and water to form alumina-depleted bridgmanite/postperovskite and phase δ-H solid solution, $AOOH-MgSiO_2(OH)_2$. The partitioning behavior

of alumina between bridgmanite and δ-H solid solution has significant implications for the seismic structure of the lower mantle because the alumina content in bridgmanite affects the sharpness and the position of the garnet-bridgmanite and postperovskite transition boundaries (Yuan et al. 2019).

Recent studies have revealed the existence of a high-pressure phase of pyrite-type FeO_2H_x as a reaction product between iron and water at 76 GPa and 1,800 K (Hu et al. 2016). Nishi et al. (2017) reported the existence of FeO_2H_x pyrite, which is close to stoichiometric. Yuan et al. (2018) observed a mixture of pyrite FeO_2H_x and dhcp-FeH_x as a reaction product of iron and water at 78 GPa and 2,000 K.

3.2. Solubility and Partitioning of Water in Nominally Anhydrous Minerals

Wadsleyite and ringwoodite can accommodate a large amount of water: 1.8–2.3 wt% and 1–1.25 wt%, respectively, at 16.5 GPa and 1,673 K (Inoue et al. 2010). Therefore, the MTZ can be the most important water reservoir in Earth's interior. Akimotoite (ilmenite $MgSiO_3$), which exists in the harzburgite layer of the slab, contains around 350–440 ppm water at 19–24 GPa and 1,573–1,873 K (Bolfan-Casanova et al. 2000).

Contradictory results exist regarding the water content of ferropericlase and bridgmanite recovered from high-pressure, high-temperature experiments. Bolfan-Casanova et al. (2002) reported that periclase and ferropericlase recovered from 25 GPa and 2,273 K contained a very small amount of water, up to 20 ppm, and Litasov & Ohtani (2003) reported 60 ppm water in alumina-bearing periclase and ferropericlase recovered from 25 GPa and 2,073 K. However, Murakami et al. (2002) reported that periclase recovered from 25.5 GPa and 1,873 K contained 1,900 ppm water. Such a high water content in periclase may be an artifact and may have originated from brucite precipitating from fluids during temperature quenching.

Controversy exists also about the water content of bridgmanite. Bolfan-Casanova et al. (2000) and Litasov et al. (2003) reported that $MgSiO_3$ bridgmanite synthesized at 24–25 GPa and 1,573–1,873 K contains almost no water, less than 1 ppm, even under water-saturated conditions. Similarly, Bolfan-Casanova et al. (2003) and Panero et al. (2015) reported that Al-Fe-bearing bridgmanite contains a very small amount of water, less than 10 ppm, at 24–26 GPa and 1,600–2,000 K. However, Murakami et al. (2002) and Litasov et al. (2003) reported that Al-Fe-bearing bridgmanite can contain 1,000–2,000 ppm water at 26 GPa and 1,500–1,923 K. Recently, Fu et al. (2019) demonstrated that a single crystal Al-Fe-bearing bridgmanite can contain 1,020 ppm water at 24 GPa and 2,073 K. Water is stored in the oxygen vacancy in bridgmanite through the reaction $2MgAlO_{2.5}$ (Brg) + H_2O (fluid) = $2MgHAlO_3$ (Brg). Thus, the $MgAlO_{2.5}$ component determines water solubility in bridgmanite. Z. Liu et al. (2017) reported that the amount of $MgAlO_{2.5}$ in bridgmanite decreases rapidly with increasing pressure and becomes negligible at 40 GPa. Both Fe^{3+} and Al^{3+}, i.e., the $FeAlO_3$ components, consume oxygen vacancies in bridgmanite and can reduce its water solubility (Liu et al. 2020). Thus, bridgmanite should be essentially dry and rheologically strong, at least in the upper part of the lower mantle. Recent ab initio simulation by Hernandez et al. (2013) suggests the possible existence of water in $MgSiO_3$ bridgmanite and postperovskite at the base of the lower mantle; however, they ignored the effect of an $FeAlO_3$ component in these phases, thus limiting the applicability of their results to the deep mantle.

Water solubility in stishovite varies significantly with temperature. The solubility of water in pure SiO_2 stishovite is very small, 15–72 ppm, at 10–24 GPa and 1,200–1,500 K (Bolfan-Casanova et al. 2000), whereas stishovite synthesized at 10 GPa and 623–823 K contains a significant amount of water: 1.3 ± 0.2 wt% (Spektor et al. 2011). Alumina-bearing stishovite contains water up to 844 ppm at 10–15 GPa and 1,473–1,673 K (Chung & Kagi 2002), whereas at 20 GPa and above 1,400 K, it contains 2,500 ppm (Litasov et al. 2007). There are no reports on water solubility in

Table 3 Water solubility in nominally anhydrous minerals

Nominally anhydrous mineral(s)	Formula	Water content	Pressure and temperature (GPa/K)	Reference(s)
Wadsleyite	Mg_2SiO_4	1.8–2.3 wt%	16.5/1,673	Inoue et al. 2010
Ringwoodite	Mg_2SiO_4	1–1.25 wt%	16.5/1,673	Inoue et al. 2010
Akimotoite	$MgSiO_3$	350~440 ppm	19~24/1,573~1,873	Bolfan-Casanova et al. 2000
Bridgmanite	$MgSiO_3$	<1 ppm	24~25/1,573~1,873	Bolfan-Casanova et al. 2000, Litasov et al. 2003
Al-Fe-bearing bridgmanite	$(MgFeAl)SiO_3$	<10 ppm	24~26/1,600~2,000	Bolfan-Casanova et al. 2003, Panero et al. 2015
Al-Fe-bearing bridgmanite	$(MgFeAl)SiO_3$	1,000–2,000 ppm	26/1,500~1,923	Murakami et al. 2002, Litasov et al. 2003
Al-Fe-bearing bridgmanite	$(MgFeAl)SiO_3$	1,020 ppm	24/2,073	Fu et al. 2019
Periclase, ferropericlase	MgO, (MgFe)O	20 ppm	25/2,273	Bolfan-Casanova et al. 2000
Periclase, ferropericlase	MgO, (MgFe)O	60 ppm	25/2,073	Litasov & Ohtani 2003
Periclase	MgO	1,900 ppm	25.5/1,873	Murakami et al. 2002
Stishovite	SiO_2	15–72 ppm	10~24/1,200~1,500	Bolfan-Casanova et al. 2000
Stishovite	SiO_2	1.3 ± 0.2 wt%	10/623–823	Spektor et al. 2011
Aluminous stishovite	$Al-SiO_2$	844 ppm	10~15/1,473~1,673	Chung & Kagi 2002
CaCl$_2$ type (not identified but estimated from experimental conditions)	SiO_2	480 ppm	60/2,600	Panero et al. 2003

poststishovite phases such as the $CaCl_2$ type and α-PbO_2 type of SiO_2, although Panero et al. (2003) reported 480 ppm water at 60 GPa and above 2,600 K in alumina-bearing SiO_2, which is likely to be $CaCl_2$-type SiO_2 based on its stability (Lakshtanov et al. 2007). The water solubility of nominally anhydrous minerals in the mantle is summarized in **Table 3**.

In order to understand the effect of water on the physical properties of major minerals that influence the properties of the bulk mantle, water partitioning studies between nominally anhydrous and hydrous minerals are essential. According to Bolfan-Casanova et al. (2003), the partition coefficient of water between ringwoodite and bridgmanite, $D_{Rg/Brg}$, is around 1,050–1,400, showing strong partitioning of water in the MTZ compared to that in the lower mantle. They also reported that the partition coefficient of water between ferropericlase and bridgmanite, $D_{Fp/Brg} = 60–75$, reflects significant partitioning of water into ferropericlase, and that water partitioning between superhydrous phase B and bridgmanite, $D_{Sb/Brg}$, is very large; i.e., the water content in bridgmanite, coexisting with superhydrous phase B, is below the detection limit of Fourier-transform infrared spectroscopy.

3.3. Effects of Water on Phase Boundaries and Mantle Discontinuities

The phase boundaries of the olivine-wadsleyite transition and the decomposition of ringwoodite (postspinel transition) are thought to correspond, respectively, to the 410-km and 660-km
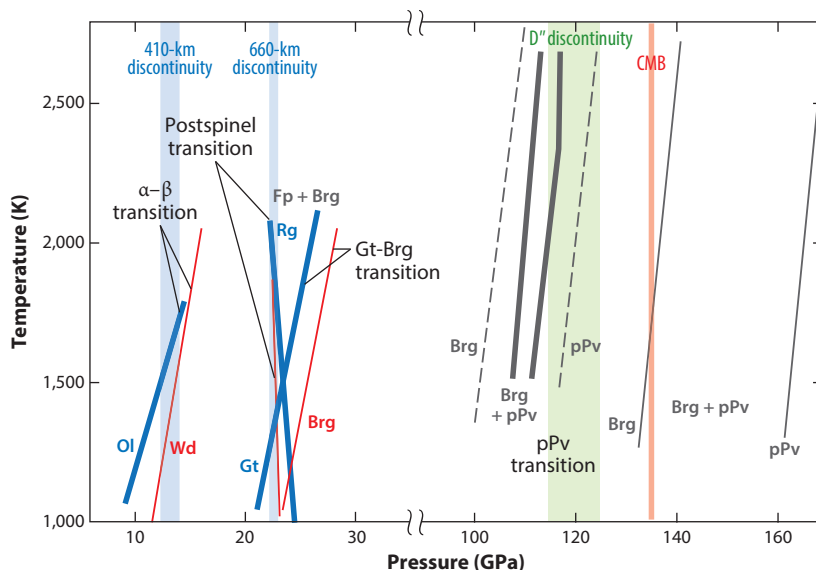
Figure 2

The effect of water on phase boundaries in the mantle. Thin red lines and thick blue lines mark the phase boundaries of the α–β transitions, postspinel transitions of Mg_2SiO_4 (Litasov et al. 2006), and Gt-Brg transitions in MORB (Sano et al. 2006) under the dry and wet conditions, respectively. Thin gray solid and dashed lines are the pPv transition boundaries for dry peridotite and dry MORB, respectively (Grocholski et al. 2012). Thick gray solid lines are the wet pPv transition boundary (Yuan et al. 2019). The 410-km and 660-km discontinuities and D″ discontinuity are shown as blue and green shaded zones, respectively. The CMB is shown as a thick orange line. Abbreviations: Brg, bridgmanite; CMB, core–mantle boundary; Fp, ferropericlase; Gt, garnet; MORB, mid-ocean ridge basalt; Ol, olivine; pPv, postperovskite; Rg, ringwoodite; Wd, wadsleyite.

discontinuities. The topography and sharpness of these discontinuities could reflect the water content in the MTZ.

The olivine-wadsleyite transition boundary has been studied extensively because the boundary has been used for estimating temperature at the 410-km discontinuity (e.g., Katsura et al. 2004). It has been estimated thermodynamically that the boundary shifts to lower pressure due to the difference in water solubility between olivine and wadsleyite. The boundary also becomes broader under wet conditions, with the thickness of the two-phase loop (the depth interval of coexistence of olivine and wadsleyite) expanding from 7 km under dry conditions to 22 km for the hydrous system containing 500 ppm water (Wood 1995). This effect of water has been confirmed experimentally by several authors. Smyth & Frost (2002) reported the boundary shifts by 1 GPa in the presence of 3 wt% water. Litasov et al. (2006) found similar results by using in situ X-ray diffraction experiments. The 410-km discontinuity thus clearly becomes shallower and broadens in wet mantle, as shown in **Figure 2**.

Decomposition of ringwoodite into ferropericlase and bridgmanite (postspinel transition) is thought to correspond to the 660-km discontinuity (e.g., Katsura et al. 2003). Recent experiments using precise in situ X-ray diffraction (Ishii et al. 2018) have revealed that the phase boundary completely matches the depth of the 660-km discontinuity. Several studies have demonstrated that the phase boundary, under wet conditions, appears to shift to higher pressure. Higo et al. (2001) reported a 0.2 GPa shift of the phase boundary at 1,873 K with 1 wt% water. Litasov et al. (2006) showed, using in situ X-ray diffraction, that the boundary in hydrous pyrolite with 2 wt% water

shifts to higher pressure by 0.6 GPa relative to anhydrous pyrolite at 1,473 K. Thus, depressions in the topography of the 660-km discontinuity could be accounted for by wetter conditions and/or lower temperatures compared to the surrounding mantle as shown in **Figure 2**.

Water can also modify the location of the garnet-bridgmanite phase boundary. Sano et al. (2006) determined the garnet-bridgmanite phase boundary in mid-ocean ridge basalt under dry and wet 10 wt% water conditions using in situ X-ray diffraction and revealed that the boundary shifts to lower pressure by 2 GPa under the wet conditions. The cause of the shift of the phase boundary may be an increase of ferric iron in garnet and bridgmanite under wet conditions with high fO_2.

The phase transition from bridgmanite to the postperovskite phase may mark the D″ layer at the base of the lower mantle (Murakami et al. 2004). However, inconsistencies between the depth and broadness of the postperovskite phase transition and the characteristics of the D″ layer have been identified (Grocholski et al. 2012). Recently, Ohira et al. (2014) revealed that the alumina content in bridgmanite in mantle peridotite drops significantly from about 6 wt% to less than 1 wt% under wet conditions, through coexistence with δ-H solid solution, resulting in a shift of the phase-transition boundary to a lower pressure and a narrowing of the transition width compared to dry alumina-enriched bridgmanite conditions (Yuan et al. 2019). A wet postperovskite boundary is consistent with the location of the D″ layer at the bottom of the lower mantle as shown in **Figure 2**.

4. EFFECTS OF WATER ON THE PHYSICAL PROPERTIES OF MINERALS

Water modifies the physical properties of mantle minerals such as electrical conductivity, sound velocity, and thermal conductivity. The effects of water on electrical conductivity were reviewed by Yoshino & Katsura (2013) and are illustrated in **Figure 3**. The water content in the mantle can also be inferred from electrical conductivity, as discussed later. This section reviews the effect of water on sound velocity and thermal conductivity in mantle minerals.

4.1. Sound Velocity

Seismic velocity is one of the most important properties for estimating water content in the mantle. Significant efforts have been made to measure the sound velocity of hydrous minerals in subducting slabs, including chlorite (Mookherjee & Mainprice 2014), serpentine (Bezacier et al. 2013), and the 23 Å phase (Cai et al. 2019). The P-wave velocity (V_P) and S-wave velocity (V_S) of these phases are significantly lower than those of the major nominally anhydrous minerals in the upper mantle.

Wadsleyite and ringwoodite can contain large amounts of water; therefore, the effect of water on the sound velocity of these minerals can be used to evaluate the water content of the MTZ. The velocity contrast in both V_P and V_S between olivine and wadsleyite reduces from 12–13% under dry conditions to 7–8% when wadsleyite has 1.5 wt% H_2O (Mao et al. 2008). Thus, the seismic velocity jump at 410 km depth is sensitive to the presence of H_2O in wadsleyite. Reduction of the sound velocity, however, can also be caused by higher temperatures or iron enrichment. Therefore, it is necessary to distinguish the effect of water from other effects.

Li et al. (2011) suggested that the seismic ratio $R = d\ln V_S/d\ln V_P$ is sensitive to hydration in Mg_2SiO_4 olivine, wadsleyite, and ringwoodite. They estimated that R_{H2O} exceeds 2 for 1 wt% H_2O. The seismic ratio due to Fe, R_{Fe}, changes by 1.4–1.5 as Fe/(Fe + Mg) changes from 0 to 0.2, while the effect of an increase in temperature from 1,273 to 1,773 K is 1.3–1.4. Buchen et al. (2018) pointed out that the seismic ratio R extrapolated to high pressures and temperatures
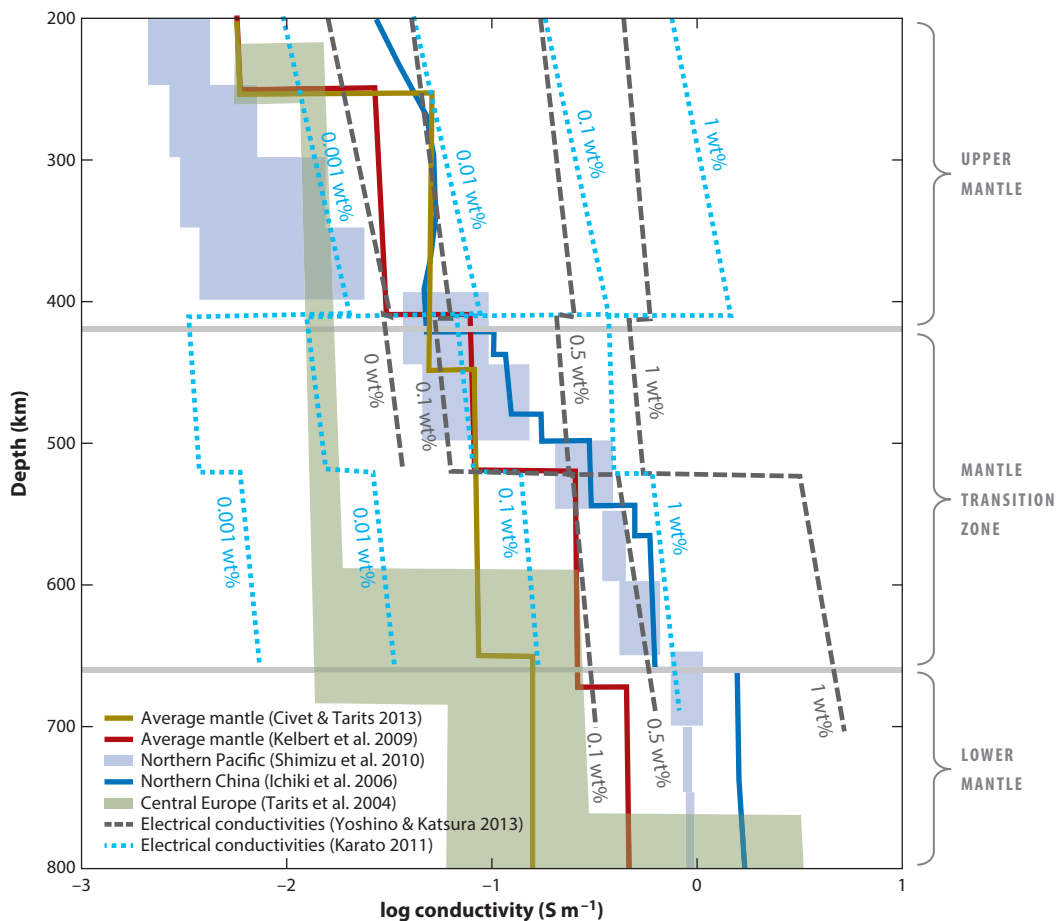
Figure 3

Electrical conductivity profiles from various localities in the mantle. Yellow and red curves are the conductivity of the average mantle reported by Civet & Tarits (2013) and Kelbert et al. (2009), respectively. Blue and green shaded areas are those of Northern Pacific and Central Europe reported by Shimizu et al. (2010) and Tarits et al. (2004), respectively. The dark blue line is the conductivity of the mantle beneath northern China reported by Ichiki et al. (2006). The electrical conductivities of olivine and its high-pressure polymorphs under the dry and wet conditions with water content up to 1 wt% are shown with dark gray dashed lines (Yoshino & Katsura 2013) and light blue dashed lines (Karato 2011).

has a large uncertainty and is inappropriate for detection of hydration in the mantle. They proposed acoustic impedance ($Z_{P,S} = V_{P,S} \times \rho$) contrasts across the olivine-wadsleyite phase boundary, $\delta Z_{P,S}/Z$(average) in percent $\{= 200[V_{P,S} \times \rho(Wd) - V_{P,S} \times \rho(Ol)]/[V_{P,S} \times \rho(Wd) + V_{P,S} \times \rho(Ol)]\}$, as sensitive measures to hydration.

The sound velocities of DHMS in the MTZ and lower mantle, including phase A (Sanchez-Valle et al. 2008), phase E (Satta et al. 2019), and phase δ-AlOOH (Mashino et al. 2016), were determined recently and found to be significantly lower than those of nominally anhydrous minerals in the MTZ and lower mantle. Ohira et al. (2019) reported a high spin–low spin transition at 30–40 GPa in δ-(Fe,Al)OOH and a bulk sound velocity anomaly associated with this transition. Ohira (2018) determined the sound velocity of δ-(Fe,Al)OOH by nuclear resonance inelastic X-ray scattering at high pressure and room temperature, and showed that the V_P of this phase

is similar or slightly lower, whereas the V_S is significantly lower than that of the preliminary reference Earth model (PREM) (Dziewonski & Anderson 1981). J. Liu et al. (2017) reported that pyrite FeOOH$_x$ has a sound velocity significantly lower than that of lower mantle minerals.

4.2. Thermal Conductivity

Water reduces the thermal conductivity of nominally anhydrous minerals. Chang et al. (2017) reported that the thermal conductivity of olivine Fo$_{90}$ with 0.7 wt% water is only half that of dry olivine at 15 GPa. Similarly, the thermal conductivity of hydrous ringwoodite with 1.72 wt% water is 40% of dry ringwoodite (Marzotto et al. 2020). Room temperature values determined experimentally can be used to estimate the thermal conductivity at other temperatures by a typical $T^{-1/2}$ dependence. Marzotto et al. (2020) argued that water affects the thermal evolution of descending slabs significantly; i.e., slabs remain relatively cool even while descending into the lower mantle, resulting in the continued stability of hydrous phases.

Hsieh et al. (2020) reported the thermal conductivity of pure δ-AlOOH and δ-(FeAl)OOH to pressures equivalent to the base of the lower mantle at room temperature. They observed a peak of the thermal conductivity associated with the spin transition of Fe^{3+} in δ-phase (FeAl)OOH at around 30–40 GPa. When δ-(FeAl)OOH forms in the slab, at the top of the lower mantle, in the presence of released water, it could create a region with higher thermal conductivity and hence a warmer region at the top of the lower mantle. The changes of thermal conductivity of δ-(FeAl)OOH with pressure are shown in **Figure 4**. The thermal conductivity of δ-(FeAl)OOH is significantly lower than that of the major minerals in the lower mantle, at the core–mantle boundary, resulting in thermal anomalies that could cause partial melting and formation of an ultra-low velocity zone (ULVZ) (Hsieh et al. 2020).
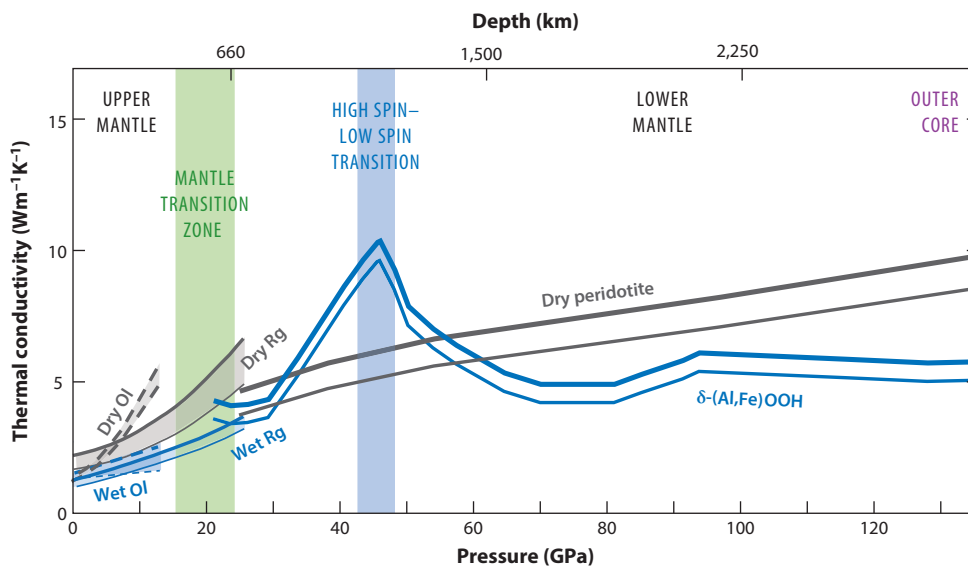

Figure 4

Thermal conductivity of dry and hydrous minerals in the mantle along the geotherm with a potential temperature of 1,600 K (*thick curves*) and 2,000 K (*thin curves*): dry and wet (0.7 wt% water) Ol (Chang et al. 2017), dry and wet (1.73 wt% water) Rg (Marzotto et al. 2020), and dry pyrolitic mantle and hydrous δ-(Al,Fe)OOH (Hsieh et al. 2020). A peak associated with the high spin–low spin transition in δ-(Al,Fe)OOH is evident. The temperature correction is made using a typical $T^{-1/2}$ dependence. Abbreviations: Ol, olivine; Rg, ringwoodite.

5. DISTRIBUTION OF WATER IN EARTH'S INTERIOR: GEOPHYSICAL OBSERVATIONS AND MINERALOGICAL CONSTRAINTS

5.1. Water-Bearing Minerals Discovered in the Mantle

It is well known that deep-seated diamonds contain inclusions of high-pressure minerals. Wirth et al. (2007) discovered hydrous phase egg ($AlSiO_3OH$) in diamond from Juina, Brazil. Pearson et al. (2014) reported hydrous ringwoodite containing 1 wt% water in diamond from the same locality. These minerals indicate the existence of water in the MTZ. Additionally, Wirth et al. (2007) and Kaminsky (2017) suggested the presence of δ-AlOOH as an inclusion in the same diamond. Phase egg is stable under wide pressure and temperature conditions in the MTZ and at the top of the lower mantle (Sano et al. 2004, Abe et al. 2018), whereas δ-AlOOH is stable to the base of the lower mantle (Duan et al. 2018).

Some inclusions in diamonds point to water in the upper mantle. Tschauner et al. (2018) discovered high-pressure water ice, Ice-VII, stable at around 2 GPa (Pruzan et al. 2003). Huang et al. (2020) reported the existence of the hydrous phase TAP that is stable in the deep upper mantle at pressures around 5–7 GPa. This phase, because its stability field has a high temperature bound, can transport water, via subducting slabs, into the deep upper mantle (Fumagalli et al. 2001). The stability conditions of these water-bearing minerals are shown in **Figure 1**.

5.2. Hydration and Dehydration in Subducting Slabs

Hydration and dehydration reactions are the most significant processes occurring in subducting slabs. Hacker et al. (2003) argued that the double seismic zone in slabs coincides with the stability field of serpentine and suggested that its dehydration produces fluids that destabilize cold slabs and trigger intermediate-depth earthquakes. Ferrand et al. (2017) pointed out that intermediate-depth earthquakes can be caused by lattice instability associated with rapid volume reduction during dehydration. These observations indicate that the water in subducting slabs is stored in hydrous minerals. van Keken et al. (2011) estimated that two-thirds of stored water is ultimately lost due to dehydration reactions generating earthquakes and island arc magmatism, and one-third is transported further, reaching depths greater than 200 km. The descending slabs contain 300–3,000 ppm water in the deep upper mantle (Hacker et al. 2003, van Keken et al. 2011, Peslier et al. 2017).

Some seismological studies have revealed low-velocity regions within subducting slabs at depths from 410 km to 660 km in the MTZ (e.g., Kawakatsu & Yoshioka 2011). The low-velocity region is referred to as the metastable olivine wedge. It results from the existence of metastable olivine and remains because of sluggish reaction kinetics at low temperatures in slabs. Based on this observation, Green et al. (2010) and Kawakatsu & Yoshioka (2011) argued that the metastable olivine wedge could reflect dry descending slabs because olivine containing water less than 300 ppm behaves according to dry kinetics (Kubo et al. 2009). The presence of metastable olivine in wet slabs is therefore paradoxical, and the hydration state of the slabs remains an open question.

5.3. Water Distribution in the Upper Mantle

As discussed, water-bearing phases have been reported as inclusions in deep-seated diamonds from the upper mantle. However, the average water content of the upper mantle is estimated to be as low as 200 ppm (Peslier et al. 2017). The electrical conductivity profiles of the upper mantle and MTZ are shown in **Figure 3**. Continental and oceanic lithospheres and asthenospheres have different water contents, which can be observed from both electrical conductivity sounding and

rock samples. The electrical conductivity profile of cratonic mantle lithosphere can be explained by the presence of dry olivine, containing less than 20 ppm water (e.g., Jones et al. 2013). The water content estimated using electrical conductivity varies with depths, from the dry oceanic lithosphere (<50 ppm) underlain by a progressively wetter asthenosphere with 400 ppm H_2O at around 300 km depth (e.g., Pommier 2014). These observations indicate that the upper mantle is generally dry, but wet domains occur locally.

5.4. Existence of a Low-Velocity Region at the Base of the Upper Mantle: A Possible Site of Dehydration Melting

There are several seismological studies reporting low-velocity regions at the bottom of the upper mantle beneath Japan and northeast China (Revenaugh & Sipkin 1994), Europe (Nolet & Zielhaus 1994), and the United States (Song et al. 2004). Tauzin et al. (2010) also reported seismic evidence for a global low-velocity layer at the base of the upper mantle. The low-velocity region may be caused by hydrous partial melts. The melting phase diagrams of hydrous peridotite (e.g., Litasov & Ohtani 2002) and the density of wet magmas (Sakamaki et al. 2009) indicate that a gravitationally stable dense hydrous melt exists at the top of the MTZ. Bercovici & Karato (2003) suggested an MTZ water filter model based on these observations. The dry solidus temperature is higher than the mantle geotherm, and water is needed to lower the solidus temperature of the mantle. Dehydration melting in the ascending wet plume occurs as a consequence of changes in the water solubility of minerals moving from the MTZ into the upper mantle (e.g., Ohtani et al. 2004).

5.5. Distribution of Water in the Mantle Transition Zone

The effect of water on phase boundaries and sound velocities in minerals in the MTZ was reported above and shown in **Figure 2**. A thick MTZ, through elevation of the 410-km discontinuity and depression of the 660-km discontinuity, may suggest both low temperatures and high water content in the MTZ. In addition, in the MTZ, low temperature will produce fast shear velocity, whereas high water content will produce slow shear velocity. Therefore, correlations between MTZ thickness and its shear velocity could constrain water content by separating the effects of temperature and water. Several seismological studies have been conducted to test these correlations. Suetsugu et al. (2010) used this procedure to estimate the water content in the stagnant slab beneath the Philippine Sea. They concluded that the slab contains more water than the surrounding normal mantle. The water content was estimated, with considerable uncertainty, to be about 0.2 wt% in this region. Similarly, Houser (2016) analyzed possible water contents by comparing the 410- and 660-km discontinuity depths with shear wave tomography within the MTZ. She estimated about 0.6 wt% water in the same part of the stagnant slabs, whereas there is no definite evidence of water in the MTZ globally, suggesting that water is distributed locally and that the MTZ is generally dry. Chambers et al. (2005) reported local variations in impedance contrasts at the 410-km discontinuity. A large V_S impedance contrast would be compatible with water content up to 0.5 wt% in wadsleyite in the MTZ (Buchen et al. 2018).

Electrical conductivity sounding is a powerful tool to estimate water content in the MTZ. **Figure 3** shows the variation in electrical conductivity observations of various parts of the MTZ, suggesting possible heterogeneity in water content. There are contradictory data sets of electrical conductivity in olivine and its high-pressure polymorphs (e.g., Karato 2011, Yoshino & Katsura 2013). However, in both cases water content in the average MTZ is estimated to be around

0.1 wt%, and a higher water content, 0.5–1 wt%, is found in the MTZ below northwestern China and the Philippine Sea.

The combination of seismic tomography and electrical conductivity sounding is a powerful tool for estimating water content in the MTZ. Koyama et al. (2006) combined analysis of three-dimensional electromagnetic (EM) tomography with V_P tomography in the MTZ along a line beneath the Philippines, the Mariana Islands, and Hawaii. They found that the water content in the MTZ is heterogeneous, and there are local high concentrations of water, around 0.3 wt%, in the MTZ beneath the Marianas. Utada et al. (2009) made similar analyses of the MTZ beneath Europe and identified a difference between two regions: The European MTZ is drier than that beneath western Pacific subduction zones.

The viscosity profile of the mantle, derived from postglacial rebound and gravity data, shows that the viscosity of the MTZ is one order of magnitude lower than the upper and lower mantles (e.g., Mitrovica & Forte 2004, Soldati et al. 2009). This observation suggests a different view of the water content in the MTZ. Fei et al. (2017) determined the dislocation mobility of dry and hydrous ringwoodite and bridgmanite and argued that the low viscosity of the MTZ can be accounted for by hydrous ringwoodite containing 1–2 wt% water. Based on this, the MTZ should be nearly water saturated globally, which contradicts the seismic and EM analyses (e.g., Utada et al. 2009, Houser 2016).

5.6. Dehydration and Hydration Sites in the Lower Mantle

There are few geophysical constraints on the global water content in the lower mantle. However, seismological studies suggest that water may exist in particular regions of the lower mantle. These are discussed with reference to the top, middle, and base of the lower mantle.

5.6.1. Top of the lower mantle.
The top of the lower mantle is a place of seismic anomalies related to the existence of volatiles or melts. Lawrence & Wysession (2006) reported global attenuation patterns around subducting slabs, indicating low Q anomalies in the shallow lower mantle beneath eastern Asia. Schmandt et al. (2014) reported the existence of a low Q and low V_S region in the shallow lower mantle beneath North America, where volatile-rich magmas may be located. They suggested that dehydration melting may result from downward flow across the 660-km discontinuity, where hydrated ringwoodite decomposes into the lower mantle assemblage and there is low water storage capacity at the top of the lower mantle. There, the fluid creates partial melts (Schmandt et al. 2014) and/or surrounding hydrated zones with δ-H solid solution, (AlFe)OOH-(MgSi)OOH (Ohira et al. 2019). Bulk sound velocity reduction and thermal conductivity increase can be expected due to the spin transition in this hydrous phase (Ohira et al. 2019, Hsieh et al. 2020).

5.6.2. Seismic reflectors in the upper part of the lower mantle.
Recent seismological observations indicate that seismic reflectors with a thickness of around 12 km occur in the upper part of the lower mantle (e.g., Kaneshima & Helffrich 1998, Niu et al. 2003). Niu et al. (2003) showed a decrease in V_S by 2–6% and an increase in density by 2–9% within the reflectors, whereas they observed no difference in V_P (<1%) between the reflector and the surrounding mantle. They argued that the seismic reflectors may be caused by subducting oceanic crustal materials. However, reflectors showing V_S reduction, no change in V_P, and an increase in density cannot be explained by dry oceanic crustal materials. Rather, these effects can be accounted for by fluid or melt films in the oceanic lithosphere subducting into the lower mantle (e.g., Ohtani & Litasov 2006). Such

fluids may be supplied by dehydration of superhydrous phase B and/or phase D in the hydrous peridotite layer of slabs (e.g., Xu & Inoue 2019).

5.6.3. Base of the lower mantle and origin of the ultra-low velocity zone and the large low-shear velocity provinces.

Seismic velocity anomalies such as the large low-shear velocity provinces (LLSVPs) and the ULVZ have been reported at the base of the lower mantle. LLSVPs have been observed under the African continent and the Pacific basin (e.g., Masters et al. 2000, Ritsema & Lekic 2020). The seismological properties of LLSVPs show low shear velocity, anti-correlation between bulk sound velocity (V_{ϕ}) and V_S, and slightly low V_P. The LLSVP may be caused by compositional anomalies, such as iron enrichment, in this region (e.g., Trampert et al. 2004). These seismic properties may also be explained by accumulation of phase δ (Mashino et al. 2016, Ohira 2018, Yuan et al. 2019). The mass of the LLSVP was estimated to be about 1.9% of the mantle (Burke et al. 2008). The seismic properties of LLSVP can be explained by the presence of 12 vol% (Ohira 2018) or 35 vol% (Mashino et al. 2016) of phase δ, which is equivalent to 1 or 2.6 ocean masses of water in this region (see **Table 1**).

A ULVZ, which shows a strong reduction of seismic velocity, has been observed at the core–mantle boundary (e.g., Garnero & Helmberger 1996). It also has greater density than the sur-rounding mantle (Rost et al. 2005). These anomalous seismic features may be caused by the exis-tence of dense magmas (Williams & Garnero 1996).

Recent seismic tomography studies have demonstrated that slabs have been subducted into the base of the lower mantle. Frost & Rost (2014) showed a correlation between the position of the descending slab and LLSVP/ULVZ. If slabs with hydrous phases or water-bearing nominally anhydrous minerals accumulate and are heated up at the bottom of the lower mantle, the released water promotes partial melting to form the ULVZ. Alternatively, water generated by dehydration of a hydrous δ-H solid solution may react with iron from the core to form an iron hydrate FeO_2H_x with a pyrite structure. V_P and V_S of this phase are significantly lower than those of the PREM, which may account for the ULVZ (J. Liu et al. 2017). Decomposition of pyrite FeO_2H_x generates H_2 and O_2 at the base of the lower mantle and might have triggered the Great Oxidation Event (Mao et al. 2017). **Figure 5** is a schematic showing the dehydration and hydration sites in the mantle.

5.7. The Core: A Potential Reservoir of Hydrogen

The water content and water budget in the mantle, as described above, are summarized in **Table 1**. The estimated water budget in the mantle is 1.3–6.9 ocean masses. For consistency with a smaller water budget Earth model, only a small amount of hydrogen is required in the core. However, a larger Earth water budget requires a hydrogen reservoir in the core equivalent to 4.8 ocean masses, as suggested by Wu et al. (2018). It is well known that the density deficit of the core relative to metallic iron or iron–nickel alloy suggests the presence of light elements in the core. Several candidates such as Si, O, S, and C have been proposed, and H is another light element candidate. Based on the density deficit of the core and its sound velocity, and assuming that the light element in the core is only hydrogen, the upper bound of hydrogen content has been estimated as more than 80 ocean masses (e.g., Terasaki et al. 2012, Ikuta et al. 2019). However, a recent study of Fe isotope fractionation between iron and silicate suggested that H is not the major light element in the core (Shahar et al. 2016). The hydrogen content of 0.06 wt% (about 7.5 ocean masses) has been estimated based on the geochemistry of terrestrial rocks and meteorites (McDonough 2014).
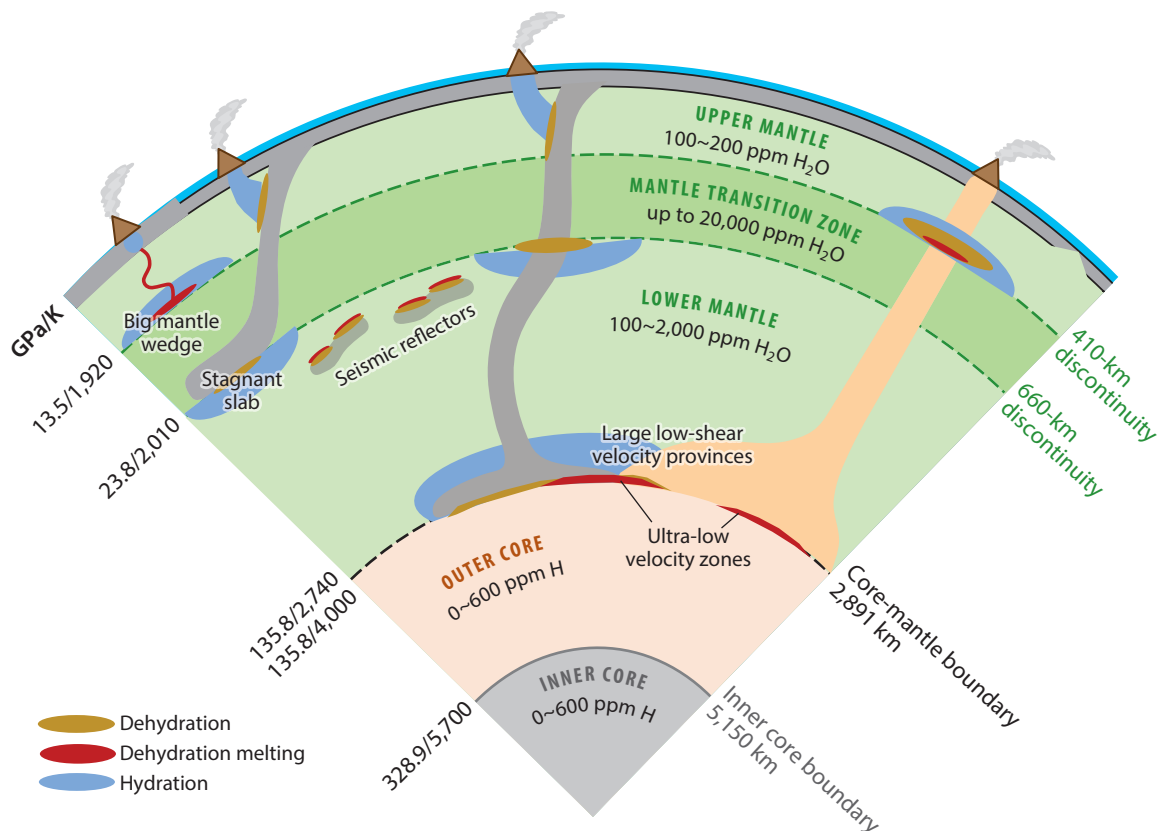
Figure 5

Location of hydration and dehydration sites in the mantle. Dehydration sites are associated with slab subduction and rising plumes. We can expect hydration sites surrounding the dehydration sites. The top and bottom of the mantle transition zone are dehydration sites due to the water solubility contrast between the upper mantle and the mantle transition zone and between the mantle transition zone and the lower mantle. The big mantle wedge (Zhao & Ohtani 2009) is also shown. Fluid/melts might exist within the seismic reflectors in the lower mantle. Dehydration/hydration regions are expected at the bottom of the lower mantle. Dense hydrous melts might exist at the bottom of both the upper mantle and the lower mantle (e.g., Sakamaki et al. 2009).

6. SUMMARY

The current understanding of Earth's water budget, water distribution, and water circulation can be summarized as follows:

1. The major source of water delivery was chondritic meteorites that arrived during accretion, giant impact, and/or late veneer stages. A smaller amount of water was delivered from the primitive solar nebula in the early stages of accretion.
2. Estimates of total water budgets vary significantly from 1–4 ocean masses in the accretional model without nebular gas to 7–12 ocean masses in the model that includes ingassing of nebular gas.
3. Earth's water budget, excluding the core, is 2.6–8.3 ocean masses. Hidden water reservoirs might exist in the core for consistency with a large water budget model, although Fe isotopic

evidence suggests the hydrogen content in the core is minor. The present estimate of the water distribution in Earth's interior is given in **Table 1**.

4. Slabs in the upper mantle are a site of dehydration, promoting earthquakes and island arc magmatism. The bottom of the upper mantle is a site of dehydration or dehydration melting resulting from changes in the water storage capacity of the constituent minerals.

5. Water is distributed heterogeneously in the MTZ, which is wetter than the upper and lower mantles. Water is concentrated locally in some regions of the MTZ near slabs.

6. There are three sites of dehydration/hydration in the lower mantle: the top, the upper/middle part, and the bottom. The region at the top of the lower mantle is defined by a large contrast between the water contents of minerals in the MTZ and those in the lower mantle. Seismic reflectors in the upper/middle lower mantle may be produced by fluid/melt in descending slabs. The base of the lower mantle is a site of dehydration and/or dehydration melting, which may be the cause of LLSVP and ULVZ. A schematic of the mantle showing dehydration/hydration sites is shown in **Figure 5**.

DISCLOSURE STATEMENT

ACKNOWLEDGMENTS

LITERATURE CITED

Abe R, Shibazaki Y, Ozawa S, Ohira I, Tobe H, Suzuki A. 2018. In situ X-ray diffraction studies of hydrous aluminosilicate at high pressure and temperature. *J. Mineral. Petrol. Sci.* 113:106–11

Abe Y, Matsui T. 1986. Early evolution of the Earth: accretion, atmosphere formation, and thermal history. *J. Geophys. Res.* 91(B13):E291–302

Alexander CMOD, Bowden R, Fogel ML, Howard KT, Herd CDK, Nittler LR. 2012. The provenances of asteroids, and their contributions to the volatile inventories of the terrestrial planets. *Science* 337:721–23

Bell DR, Ihinger PD. 2000. The isotopic composition of hydrogen in nominally anhydrous mantle minerals. *Geochim. Cosmochim. Acta* 64:2109–18

Bercovici D, Karato S. 2003. Whole-mantle convection and the transition zone water filter. *Nature* 425:39–44

Bezacier L, Reynard B, Cardon H, Montagnac G, Bass J. 2013. High-pressure elasticity of serpentine and seismic properties of the hydrated mantle wedge. *J. Geophys. Res. Solid Earth* 118:527–35

Bockelée-Morvan D, Calmonte U, Charnley S, Duprat J, Engrand C, et al. 2015. Cometary isotopic measurements. *Space Sci. Rev.* 197:47–83

Bolfan-Casanova N, Keppler H, Rubie DC. 2000. Water partitioning between nominally anhydrous minerals in the $MgO–SiO_2–H_2O$ system up to 24 GPa: implications for the distribution of water in the Earth's mantle. *Earth Planet. Sci. Lett.* 182:209–21

Bolfan-Casanova N, Keppler H, Rubie DC. 2003. Water partitioning at 660 km depth and evidence for very low water solubility in magnesium silicate perovskite. *Geophys. Res. Lett.* 30:1905

Bolfan-Casanova N, Mackwell S, Keppler H, McCammon C, Rubie DC. 2002. Pressure dependence on H solubility in magnesiowüstite up to 25 GPa: implications for the storage of water in the Earth's lower mantle. *Geophys. Res. Lett.* 29(10):89-1–89-4

Buchen J, Marquart H, Speziale S, Kawazoe T, Boffa Ballan T, Kurnosov A. 2018. High-pressure single-crystal elasticity of wadsleyite and the seismic signature of water in the shallow transition zone. *Earth Planet. Sci. Lett.* 498:77–87

Burke K, Steinberger B, Torsvik TH, Smethurst MA. 2008. Plume generation zones at the margins of large low shear velocity provinces on the core–mantle boundary. *Earth Planet. Sci. Lett.* 265:49–60

Cai N, Chen T, Qi X, Inoue T, Li B. 2019. Sound velocities of the 23 Å phase at high pressure and implications for seismic velocities in subducted slabs. *Phys. Earth Planet. Inter.* 288:1–8

Cai N, Inoue T, Fujino K, Ohfuji H, Yurimoto H. 2015. A possible new Al-bearing hydrous Mg-silicate (23 angstrom phase) in the deep upper mantle. *Am. Mineral.* 100:2330–35

Chambers K, Deuss A, Woodhouse JH. 2005. Reflectivity of the 410 km discontinuity from *PP* and *SS* precursors. *J. Geophys. Res.* 110(B2):B02301

Chang YY, Hsieh WP, Tan E, Chen J. 2017. Hydration-reduced lattice thermal conductivity of olivine in Earth's upper mantle. *PNAS* 114(16):4078–81

Chung JI, Kagi H. 2002. High concentration of water in stishovite in the MORB system. *Geophys. Res. Lett.* 29:16-1–16-4

Civet F, Tarits P. 2013. Analysis of magnetic satellite data to infer the mantle electrical conductivity of telluric planets in the solar system. *Planet. Space Sci.* 84:102–11

Duan Y, Sun N, Wang S, Li X, Guo X, et al. 2018. Phase stability and thermal equation of state of δ-AlOOH: implication for water transportation to the Deep Lower Mantle. *Earth Planet. Sci. Lett.* 494:92–98

Dziewonski AM, Anderson DL. 1981. Preliminary reference Earth model. *Phys. Earth Planet. Inter.* 25:297–356

Eggleton RA, Boland JN, Ringwood AE. 1978. High pressure synthesis of a new aluminum silicate: $Al_5Si_5O_{17}(OH)$. *Geochem. J.* 12:191–94

Fei H, Yamazaki D, Sakurai M, Miyajima N, Ohfuji H, et al. 2017. A nearly water-saturated mantle transition zone inferred from mineral viscosity. *Sci. Adv.* 3:e1603024

Ferrand TP, Hilairet N, Incel S, Deldicque D, Labrosse L, et al. 2017. Dehydration-driven stress transfer triggers intermediate-depth earthquakes. *Nat. Commun.* 8:15247

Frost DA, Rost S. 2014. The P-wave boundary of the Large-Low Shear Velocity Province beneath the Pacific. *Earth Planet. Sci. Lett.* 403:380–92

Fu S, Yang J, Karato S, Gavrilliuk AG, Ivanova AG, et al. 2019. Water concentration in single-crystal (Al,Fe)-bearing bridgmanite grown from the hydrous melt: implications for dehydration melting at the topmost lower mantle. *Geophys. Res. Lett.* 46:10358–66

Fumagalli P, Stixrude L, Poli S, Snyder D. 2001. The 10 Å phase: a high-pressure expandable sheet silicate during subduction of hydrated lithosphere. *Earth Planet. Sci. Lett.* 186:125–41

Garnero EJ, Helmberger DV. 1996. Seismic detection of a thin lateral varying boundary layer at the base of the mantle beneath the central-Pacific. *Geophys. Res. Lett.* 23:977–80

Geiss J, Gloeckler G. 2003. Isotopic composition of H, He and Ne in the protosolar cloud. In *Solar System History from Isotopic Signatures of Volatile Elements*, ed. R Kallenbach, T Encrenaz, J Geiss, K Mauersberger, TC Owen, F Robert, pp. 3–18. Dordrecht, Neth.: Springer

Gemmi M, Fischer J, Merlini M, Poli S, Fumagalli P, et al. 2011. A new hydrous Al-bearing pyroxene as a water carrier in subduction zones. *Earth Planet. Sci. Lett.* 310:422–28

Gemmi M, Merlini M, Palatinus L, Fumagalli P, Hanfland M. 2016. Electron diffraction determination of 11.5 Å and HySo structures: candidate water carriers to the Upper Mantle. *Am. Mineral.* 101:2645–54

Green HW II, Chen WP, Brudzinski MR. 2010. Seismic evidence of negligible water carried below 400-km depth in subducting lithosphere. *Nature* 467:828–31

Grocholski B, Catalli K, Shim S, Prakapenka V. 2012. Mineralogical effects on the detectability of the post-perovskite boundary. *PNAS* 109:2275–79

Hacker BR, Peacock SM, Abers GA, Holloway SD. 2003. Subduction factory 2. Are intermediate-depth earthquakes in subducting slabs linked to metamorphic dehydration reactions? *J. Geophys. Res.* 108(B1):2030

Hallis LJ. 2017. D/H ratios of the inner Solar System. *Philos. Trans. R. Soc. A* 375:20150390

Hallis LJ, Huss GR, Nagashima K, Taylor GL, Halldórsson SA, et al. 2015. Evidence for primordial water in Earth's deep mantle. *Science* 350:795–97

Hartogh P, Lis DC, Bockelee-Morvan D, de Val-Borro M, Biver N, et al. 2011. Ocean-like water in the Jupiter family comet 103P/Hartley 2. *Nature* 478:218–20

Hayashi C, Nakazawa K, Mizuno H. 1979. Earth's melting due to the blanketing effect of the primordial dense atmosphere. *Earth Planet. Sci. Lett.* 43:22–28

Hernandez ER, Alfe D, Brodholt J. 2013. The incorporation of water into lower-mantle perovskites: a first-principles study. *Earth Planet. Sci. Lett.* 364:37–43

Higo Y, Inoue T, Irifune T, Yurimoto H. 2001. Effect of water on the spinel-postspinel transformation in Mg_2SiO_4. *Geophys. Res. Lett.* 28:3505–8

Houser C. 2016. Global seismic data reveal little water in the mantle transition zone. *Earth Planet. Sci. Lett.* 448:94–101

Hsieh WP, Ishii T, Chao KH, Tsuchiya J, Deschamps JF, Ohtani E. 2020. Spin transition of iron in δ-(Al,Fe)OOH induces thermal anomalies in Earth's lower mantle. *Geophys. Res. Lett.* 47:e2020GL087036

Hu Q, Kim DY, Yang W, Yang L, Meng Y, et al. 2016. FeO_2 and FeO_2H under deep lower mantle conditions and Earth's oxygen–hydrogen cycles. *Nature* 534:241–44

Huang S, Tschauner O, Yang S, Humayun M, Liu W, et al. 2020. HIMU geochemical signature originating from the transition zone. *Earth Planet. Sci. Lett.* 542:116323

Ichiki M, Baba K, Obayashi M, Utada H. 2006. Water content and geotherm in the upper mantle above the stagnant slab: interpretation of electrical conductivity and seismic P-wave velocity models. *Phys. Earth Planet. Inter.* 155:1–15

Ikuta D, Ohtani E, Sano-Furukawa A, Shibazaki Y, Terasaki H, et al. 2019. Interstitial hydrogen atoms in face-centered cubic iron in the Earth's core. *Sci. Rep.* 9:7108

Inoue T, Wada T, Sasaki R, Yurimoto H. 2010. Water partitioning in the Earth's mantle. *Phys. Earth Planet. Sci.* 183:245–51

Ishii T, Huang R, Fei H, Koemets I, Liu Z, et al. 2018. Complete agreement of the post-spinel transition with the 660-km seismic discontinuity. *Sci. Rep.* 8:6357

Jones AG, Muller MR, Fishwick S, Evans RL, Fullea J. 2013. Velocity-conductivity relations for cratonic lithosphere and their application: example of southern Africa. *Geochem. Geophys. Geosyst.* 14:806–27

Kaminsky FV. 2017. *The Earth's Lower Mantle: Composition and Structure*. Cham, Switz.: Springer

Kaneshima S, Helffrich G. 1998. Detection of lower mantle scatterers northeast of the Mariana subduction zone using short-period array data. *J. Geophys. Res.* 103(B3):4825–38

Kanzaki M. 1991. Stability of hydrous magnesium silicates in the mantle transition zone. *Phys. Earth Planet. Inter.* 66:307–12

Karato S. 2011. Water distribution across the mantle transition zone and its implications for global material circulation. *Earth Planet. Sci. Lett.* 301:413–23

Katsura T, Yamada H, Nishikawa O, Song M, Kubo A, et al. 2004. Olivine-wadsleyite transition in the system $(Mg,Fe)_2SiO_4$. *J. Geophys. Res.* 109(B2):B02209

Katsura T, Yamada H, Shinmei T, Kubo A, Ono S, et al. 2003. Post-spinel transition in Mg_2SiO_4 determined by high *P–T* in situ X-ray diffractometry. *Phys. Earth Planet. Inter.* 136:11–24

Kawakatsu H, Yoshioka S. 2011. Metastable olivine wedge and deep dry cold slab beneath southwest Japan. *Earth Planet. Sci. Lett.* 303:1–10

Kelbert A, Schultz A, Egbert G. 2009. Global electromagnetic induction constraints on transition-zone water content variations. *Nature* 460:1003–6

Korenaga J. 2011. Thermal evolution with a hydrating mantle and the initiation of plate tectonics in the early Earth. *J. Geophys. Res.* 116(B12):B12403

Koyama T, Shimizu H, Utada H, Ichiki M, Ohtani E, Hae R. 2006. Water contents in the mantle transition zone beneath the north Pacific derived from the electrical conductivity anomaly. In *Geophys. Monogr. Ser.* 168:171–79

Kubo T, Kaneshima S, Torii Y, Yoshioka S. 2009. Seismological and experimental constraints on metastable phase transformations and rheology of the Mariana slab. *Earth Planet. Sci. Lett.* 287:12–23

Lakshtanov DL, Sinogeikin SV, Litasov KD, Prakapenka VB, Hellwi H, et al. 2007. The post-stishovite phase transition in hydrous alumina-bearing SiO_2 in the lower mantle of the earth. *PNAS* 104(34):13588–90

Lawrence JF, Wysession ME. 2006. Seismic evidence for subduction-transported water in the lower mantle. In *Geophys. Monogr. Ser.* 168:251–61

Li L, Weidner DJ, Brodholt JP, Alfe D. 2011. Prospecting for water in the transition zone: d ln(*Vs*)/d ln(*Vp*). *Phys. Earth Planet. Inter.* 189:117–20

Litasov KD, Kagi H, Shatzky A, Ohtani E, Lakshtanov DL, et al. 2007. High hydrogen solubility in Al-rich stishovite and water transport in the lower mantle. *Earth Planet. Sci. Lett.* 262:620–34

Litasov KD, Ohtani E. 2002. Phase relations and melt compositions in CMAS–pyrolite–H_2O system up to 25 GPa. *Phys. Earth Planet. Inter.* 134:105–27

Litasov KD, Ohtani E. 2003. Hydrous lower mantle: the water source for wet plumes? In *8th International Kimberlite Conference*, FLA030. Victoria, BC: Elsevier

Litasov KD, Ohtani E, Langenhorst F, Yurimoto H, Kubo T, Kondo T. 2003. Water solubility in Mg-perovskites and water storage capacity in the lower mantle. *Earth Planet. Sci. Lett.* 211:189–203

Litasov KD, Ohtani E, Sano A. 2006. Influence of water on major phase transitions in the Earth's mantle. In *Geophys. Monogr. Ser.* 168:95–111

Liu J, Hu Q, Kim DY, Wu Z, Wang W, et al. 2017. Hydrogen-bearing iron peroxide and the origin of ultralow-velocity zones. *Nature* 551:494–97

Liu L. 1987. Effects of H_2O in the phase behavior of the forsterite-enstatite system at high pressures and temperatures and implications for the Earth. *Phys. Earth Planet. Inter.* 49:142–67

Liu Z, Ishii T, Katsura T. 2017. Rapid decrease of $MgAlO_{2.5}$ component in bridgmanite with pressure. *Geochem. Perspect. Lett.* 5:12–18

Liu Z, McCammon C, Wang B, Dubrovinsky L, Ishii T, et al. 2020. Stability and solubility of the $FeAlO_3$ component in bridgmanite at uppermost lower mantle conditions. *J. Geophys. Res.* 125:e2019jB18447

Mao H-K, Hu Q, Yang L, Liu J, Kim DY, et al. 2017. When water meets iron at Earth's core–mantle boundary. *Natl. Sci. Rev.* 4:870–78

Mao Z, Jacobsen SD, Jiang F, Smyth JR, Holl CM, et al. 2008. Single-crystal elasticity of wadsleyites, β-Mg_2SiO_4 containing 0.37–1.66 wt% H_2O. *Earth Planet. Sci. Lett.* 266:78–89

Marty B. 2012. The origins and concentrations of water, carbon, nitrogen and noble gases on Earth. *Earth Planet. Sci. Lett.* 313–314:56–66

Marty B, Yokouchi R. 2006. Water in the early Earth. *Rev. Mineral. Geochem.* 62:421–50

Marzotto E, Hsieh WP, Ishii T, Chao KH, Golabeck GJ, et al. 2020. Effect of water on lattice thermal conductivity of ringwoodite and its implications for the thermal evolution of descending slabs. *Geophys. Res. Lett.* 47:e2020GL087607

Mashino I, Murakimi M, Ohtani E. 2016. Sound velocities of δ-AlOOH up to core-mantle boundary pressures with implications for the seismic anomalies in the deep mantle. *J. Geophys. Res. Solid Earth* 121:595–609

Masters G, Laske G, Bolton H, Dziewonski A. 2000. The relative behavior of shear velocity, bulk sound speed, and compressional velocity in the mantle: implications for chemical and thermal structure. In *Geophys. Monogr. Ser.* 117:63–87

McDonough WF. 2014. Compositional model for the Earth's core. *Treatise Geochem.* 2:559–77

Mitrovica JX, Forte AM. 2004. A new inference of mantle viscosity based upon joint inversion of convection and glacial isostatic adjustment data. *Earth Planet. Sci. Lett.* 225:177–89

Mookherjee M, Mainprice D. 2014. Unusually large shear wave anisotropy for chlorite in subduction zone settings. *Geophys. Res. Lett.* 41:1506–13

Morbidelli A, Lunine JI, O'Brien DP, Raymond SN, Walsh KJ. 2012. Building terrestrial planets. *Annu. Rev. Earth Planet. Sci.* 40:251–75

Murakami M, Hirose K, Kawamura K, Sata N, Ohishi Y. 2004. Post-perovskite phase transition in $MgSiO_3$. *Science* 304:855–58

Murakami M, Hirose K, Yurimoto H, Nakashima S, Takafuji N. 2002. Water in Earth's lower mantle. *Science* 295:1885–87

Mysen B. 2018. Redox-controlled mechanisms of C and H isotope fractionation between silicate melt and COH fluid in the Earth's interior. *Prog. Earth Planet. Sci.* 5:46

Mysen B. 2019. Nitrogen in the Earth: abundance and transport. *Prog. Earth Planet. Sci.* 6:38

Nakagawa T, Iwamori H, Yanagi R, Nakano A. 2018. On the evolution of the water ocean in the plate-mantle system. *Prog. Earth Planet. Inter.* 5:51

Nishi M, Irifune T, Tsuchita J, Tange Y, Nishihara Y, et al. 2014. Stability of hydrous silicate at high pressures and water transport to the deep lower mantle. *Nat. Geosci.* 7:224–27

Nishi M, Kuwayama Y, Tsuchiya J, Tsuchiya T. 2017. The pyrite-type high-pressure form of FeOOH. *Nature* 547:205–8

Niu F, Kawakatsu H, Fukao Y. 2003. A slightly dipping and strong seismic reflector at mid-mantle depth beneath the Mariana subduction zone. *J. Geophys. Res.* 108:2419

Nolet G, Zielhaus A. 1994. Low S velocities under the Tornquist Teisseyre zone: evidence for water injection into the transition zone by subduction. *J. Geophys. Res.* 99(B8):15813–20

Ohira I. 2018. *Experimental study of δ-AlOOH–ε-FeOOH–Phase H solid solution toward understanding the water transport and seismic anomaly in the lower mantle*. PhD Thesis, Tohoku Univ., Sendai, Japan

Ohira I, Jackson JM, Solomatova NV, Sturhan W, Finkelstein GJ, et al. 2019. Compressional behavior and spin state of δ-(Al,Fe)OOH at high pressures. *Am. Mineral.* 104:1273–84

Ohira I, Ohtani E, Sakai T, Miyahara M, Hirao N, et al. 2014. Stability of a hydrous δ-phase, AlOOH–MgSiO$_2$(OH)$_2$, and a mechanism of water transport into the base of lower mantle. *Earth Planet. Sci. Lett.* 401:12–17

Ohtani E, Amaike Y, Kamada S, Sakamaki T, Hirao N. 2014. Stability of hydrous phase H MgSiO$_4$H$_2$ under lower mantle conditions. *Geophys. Res. Lett.* 41:8283–87

Ohtani E, Litasov KD. 2006. The effect of water on mantle phase transitions. *Rev. Mineral. Geochem.* 62:397–420

Ohtani E, Litasov KD, Hosoya T, Kubo T, Kondo T. 2004. Water transport into the deep mantle and formation of a hydrous transition zone. *Phys. Earth Planet. Inter.* 143–144:255–69

Ohtani E, Mizobata H, Kudoh Y, Nagase T, Arashi H, et al. 1997. A new hydrous silicate, a water reservoir, in the upper part of the lower mantle. *Geophys. Res. Lett.* 24:1047–50

Ohtani E, Toma M, Kubo T, Kondo T, Kato T, Kikegawa T. 2003. In situ X-ray observation of decomposition of superhydrous phase B at high pressure and temperature. *Geophys. Res. Lett.* 30:1029–32

Ohtani E, Yuan L, Ohira I, Shatsliy A, Litasov KD. 2018. Fate of water transported into the deep mantle by slab subduction. *J. Asian Earth Sci.* 167:2–10

Olsen P, Sharp ZD. 2019. Nebular atmosphere to magma ocean: a model for volatile capture during Earth accretion. *Phys. Earth Planet. Inter.* 294:106294

Pacalo REG, Parise JB. 1992. Crystal structure of superhydrous B, a hydrous magnesium silicate synthesized at 1400°C and 20 GPa. *Am. Mineral.* 77:681–84

Panero WR, Benedetti LR, Jeanloz R. 2003. Transport of water into the lower mantle: role of stishovite. *J. Geophys. Res.* 108(B1):2039

Panero WR, Pigott JS, Reaman DM, Kabbes JE, Liu Z. 2015. Dry (Mg,Fe)SiO$_3$ perovskite in the Earth's lower mantle. *J. Geophys. Res. Solid Earth* 120:894–908

Peacock SM. 1990. Fluid processes in subduction zone. *Science* 248:329–37

Pearson DG, Brenker FE, Nestola F, McNeill J, Nasdala L, et al. 2014. Hydrous mantle transition zone indicated by ringwoodite included within diamond. *Nature* 507(7491):221–24

Peslier AH, Schönbächler M, Busemann H, Karato S. 2017. Water in the Earth's interior: distribution and origin. *Space Sci. Rev.* 212:743–810

Pommier A. 2014. Interpretation of magnetotelluric results using laboratory measurements. *Surv. Geophys.* 35:41–84

Pruzan P, Chervin JC, Wolanin E, Canny B, Gauthier M, Hanfland M. 2003. Phase diagram of ice in the VII–VIII–X domain: vibrational and structural data for strongly compressed ice VIII. *J. Raman Spectrosc.* 34:591–610

Revenaugh J, Sipkin SA. 1994. Seismic evidence for silicate melt atop the 410-km mantle discontinuity. *Nature* 369:474–76

Ringwood AE, Major A. 1967. High-pressure reconnaissance investigations in the system Mg$_2$SiO$_4$-MgO-H$_2$O. *Earth Planet. Sci. Lett.* 2:130–33

Ritsema J, Lekic V. 2020. Heterogeneity of seismic wave velocity in Earth's mantle. *Annu. Rev. Earth Planet. Sci.* 48:377–401

Robert F. 2006. Solar system deuterium/hydrogen ratio. In *Meteorites and the Early Solar System II*, ed. DS Lauretta, HY McSween Jr., pp. 341–51. Tucson: Univ. Ariz. Press

Rost S, Garnero EJ, Williams Q, Manga M. 2005. Seismic constraints on a possible plume root at the core–mantle boundary. *Nature* 435:666–69

Rubey WW. 1951. Geologic history of seawater: an attempt to state the problem. *GSA Bull.* 62:1111–48

Rubie DC, Jacobson SA, Morbidelli A, O'Brien DP, Young ED, et al. 2015. Accretion and differentiation of the terrestrial planets with implications for the compositions of early-formed Solar System bodies and accretion of water. *Icarus* 248:89–108

Sakamaki T, Ohtani E, Urakawa S, Suzuki A, Katayama Y. 2009. Measurement of hydrous peridotite magma density at high pressure using the X-ray absorption method. *Earth Planet. Sci. Lett.* 287:293–97

Sanchez-Valle C, Sinogeikin SV, Smyth JR, Bass JD. 2008. Sound velocities and elasticity of DHMS phase A to high pressure and implications for seismic velocities and anisotropy in subducted slabs. *Phys. Earth Planet. Inter.* 170:229–39

Sano A, Ohtani E, Kubo T, Funakoshi K. 2004. In situ X-ray observation of decomposition of hydrous aluminum silicate $AlSiO_3OH$ and aluminum oxide hydroxide δ-AlOOH at high pressure and temperature. *J. Phys. Chem. Solids* 65:1547–54

Sano A, Ohtani E, Litasov K, Kubo T, Hosoya T, et al. 2006. In situ X-ray diffraction study of the effect of water on the garnet–perovskite transformation in MORB and implications for the penetration of oceanic crust into the lower mantle. *Phys. Earth Planet. Inter.* 159:118–26

Satta N, Marquardt H, Kurnosov A, Buchen J, Kawazoe T, et al. 2019. Single-crystal elasticity of iron-bearing phase E and seismic detection of water in Earth's upper mantle. *Am. Mineral.* 104:1526–29

Schmandt B, Jacobsen SD, Becker TW, Liu Z, Ducker KG. 2014. Dehydration melting at the top of the lower mantle. *Science* 344:1265–68

Schmidt MW. 1995. Lawsonite: upper pressure stability and formation of higher density hydrous phases. *Am. Mineral.* 80:1286–92

Shahar A, Schauble EA, Caracas R, Gleason AE, Reagan MM, et al. 2016. Pressure-dependent isotopic composition of iron alloys. *Science* 352:580–82

Sharp ZD. 2017. Nebular ingassing as a source of volatiles to the terrestrial planets. *Chem. Geol.* 448:137–50

Shimizu H, Koyama T, Baba H, Utada H. 2010. Revised 1-D mantle electrical conductivity structure beneath the north Pacific. *Geophys. J. Int.* 180:1030–48

Smyth JR, Frost D. 2002. The effect of water on the 410-km discontinuity: an experimental study. *Geophys. Res. Lett.* 29:GL014418

Soldati G, Boschi L, Deschamps F, Giardini D. 2009. Inferring radial models of mantle viscosity from gravity (GRACE) data and an evolutionary algorithm. *Phys. Earth Planet. Inter.* 176:19–32

Song TRA, Helmberger DV, Grand SP. 2004. Low-velocity zone atop the 410-km seismic discontinuity in the northwestern United States. *Nature* 427:530–33

Spektor K, Nylen J, Stoyanov E, Navrotsky A, Hervig RL, et al. 2011. Ultrahydrous stishovite from high-pressure hydrothermal treatment of SiO_2. *PNAS* 108(52):20918–22

Suetsugu D, Inoue T, Obayashi M, Yamada A, Shiobara H, et al. 2010. Depths of the 410-km and 660-km discontinuities in and around the stagnant slab beneath the Philippine Sea: Is water stored in the stagnant slab? *Phys. Earth Planet. Inter.* 183:270–79

Suetsugu D, Inoue T, Yamada A, Zhao D, Obayashi M. 2006. Towards mapping the three-dimensional distribution of water in the transition zone from P-velocity tomography and 660-km discontinuity depths. In *Geophys. Monogr. Ser.* 168:237–49

Suzuki A, Ohtani E, Kamada T. 2000. A new hydrous phase δ-AlOOH synthesized at 21 GPa and 1000°C. *Phys. Chem. Miner.* 27:689–93

Tarits P, Hautot S, Perrier F. 2004. Water in the mantle: results from electrical conductivity beneath the French Alps. *Geophys. Res. Lett.* 31:L06612

Tauzin B, Bebayle E, Wittlinger G. 2010. Seismic evidence for a global low-velocity layer within the Earth's upper mantle. *Nat. Geosci.* 3:718–21

Terasaki H, Ohtani E, Sakai T, Kamada S, Asanuma H, et al. 2012. Stability of Fe–Ni hydride after the reaction between Fe–Ni alloy and hydrous phase (δ-AlOOH) up to 1.2 Mbar: possibility of H contribution to the core density deficit. *Phys. Earth Planet. Inter.* 194–195:18–24

Trampert J, Deschamps F, Resovsky J, Yuen D. 2004. Probabilistic tomography maps chemical heterogeneities throughout the lower mantle. *Science* 306:853–56

Tschauner O, Huang S, Greenberg E, Prakapenka V, Ma C, et al. 2018. Ice-VII inclusions in diamonds: evidence for aqueous fluid in Earth's deep mantle. *Science* 359:1136–39

Utada H, Koyama T, Obayashi M, Fukao Y. 2009. A joint interpretation of electromagnetic and seismic tomography models suggests the mantle transition zone below Europe is dry. *Earth Planet. Sci. Lett.* 281:249–57

van Keken PE, Hacker BR, Syracuse EM, Abers GA. 2011. Subduction factory: 4. Depth-dependent flux of H_2O from subducting slabs worldwide. *J. Geophys. Res.* 116(B1):B01401

Wallace PJ. 2005. Volatiles in subduction zone magmas: concentrations and fluxes based on melt inclusion and volcanic gas data. *J. Volcanol. Geotherm. Res.* 140:217–40

Williams Q, Garnero EJ. 1996. Seismic evidence for partial melt at the base of the Earth's mantle. *Science* 273:1528–30

Wirth R, Vollmer C, Brenker F, Matsyuk S, Kaminsky F. 2007. Inclusions of nanocrystalline hydrous aluminium silicate "Phase Egg" in superdeep diamonds from Juina (Mato Grosso State, Brazil). *Earth Planet. Sci. Lett.* 259:384–99

Wood BJ. 1995. The effect of H_2O on the 410-kilometer seismic discontinuity. *Science* 268:74–76

Wu J, Desch SJ, Schaefer L, Elkins-Tanton LT, Pahlevan K, Buseck PR. 2018. Origin of Earth's water: chondritic inheritance plus nebular ingassing and storage of hydrogen in the core. *J. Geophys. Res. Planets* 123:2691–712

Xu C, Inoue T. 2019. Melting of Al-rich phase D up to the uppermost lower mantle and transportation of H_2O to the deep Earth. *Geochem. Geophys. Geosyst.* 20:4382–89

Yoshino T, Katsura T. 2013. Electrical conductivity of mantle minerals: role of water in conductivity anomalies. *Annu. Rev. Earth Planet. Sci.* 41:605–28

Yuan H, Zhang L, Ohtani E, Meng Y, Greenberg E, Prakapenka VB. 2019. Stability of Fe-bearing hydrous phases and element partitioning in the system $MgO–Al_2O_3–Fe_2O_3–SiO_2–H_2O$ in Earth's lowermost mantle. *Earth Planet. Sci. Lett.* 524:115714

Yuan L, Ohtani E, Ikuta D, Kamada S, Tsuchiya J, et al. 2018. Chemical reactions between Fe and H_2O up to megabar pressures and implications for water storage in the Earth's mantle and core. *Geophys. Res. Lett.* 45:1330–38

Zhao D, Ohtani E. 2009. Deep slab subduction and dehydration and their geodynamic consequences: evidence from seismology and mineral physics. *Gondwana Res.* 16:401–13